The $^{14}C(n,\gamma)$ cross section between 10 keV and 1 MeV

R. Reifarth,[1,*] M. Heil,[2,*] C. Forssén,[3,4] U. Besserer,[5] A. Couture,[1] S. Dababneh,[2,†] L. Dörr,[5] J. Görres,[6] R.C. Haight,[1] F. Käppeler,[2] A. Mengoni,[7] S. O'Brien,[6] N. Patronis,[8,‡] R. Plag,[2,§] R.S. Rundberg,[1] M. Wiescher,[6] and J.B. Wilhelmy[1]

[1]*Los Alamos National Laboratory, Los Alamos, New Mexico, 87545, USA*
[2]*Forschungszentrum Karlsruhe, Institut für Kernphysik, P.O. Box 3640, D-76021 Karlsruhe, Germany*
[3]*Lawrence Livermore National Laboratory, Livermore, California, 94550, USA*
[4]*Fundamental Physics, Chalmers University of Technology, 412 96 Göteborg, Sweden*
[5]*Forschungszentrum Karlsruhe, Tritiumlabor, P.O. Box 3640, D-76021 Karlsruhe, Germany*
[6]*University of Notre Dame, Physics Department, Notre Dame, IN 46556, USA*
[7]*CERN, CH-1211 Geneva 23, Switzerland*
[8]*Nucl. Phys. Lab., Department of Physics, The University of Ioannina, 45110 Ioannina, Greece*

(Dated: October 1, 2009)

The neutron capture cross section of ^{14}C is of relevance for several nucleosynthesis scenarios such as inhomogeneous Big Bang models, neutron induced CNO cycles, and neutrino driven wind models for the r process. The $^{14}C(n,\gamma)$ reaction is also important for the validation of the Coulomb dissociation method, where the (n,γ) cross section can be indirectly obtained via the time-reversed process. So far, the example of ^{14}C is the only case with neutrons where both, direct measurement and indirect Coulomb dissociation, have been applied. Unfortunately, the interpretation is obscured by discrepancies between several experiments and theory. Therefore, we report on new direct measurements of the $^{14}C(n,\gamma)$ reaction with neutron energies ranging from 20 to 800 keV.

PACS numbers: 28.20.Fc, 24.50.+g, 26.35.+c, 97.10.Cv, 98.80.Ft

I. INTRODUCTION

Inhomogeneous big bang models [1] offer the possibility to bridge the mass gaps at $A = 5$ and 8 and to contribute substantially to the synthesis of heavier nuclei. The suggested reaction sequence [2, 3] for this outbreak is ^{7}Li$(n,\gamma)^8$Li$(\alpha,n)^{11}$B$(n,\gamma)^{12}$B$(\beta^-)^{12}$C. Subsequent neutron captures on ^{12}C and ^{13}C will then lead to the production of ^{14}C, which has a half-life of 5700±30 yr [4]. On the time scale of big bang nucleosynthesis ^{14}C can be considered as stable and further proton, alpha, deuteron, and neutron capture reactions on ^{14}C will result in the production of heavier nuclei with $A \geq 20$ [2]. Due to the high neutron abundance the $^{14}C(n,\gamma)^{15}$C reaction is expected to compete strongly with other reaction channels.

The $^{14}C(n,\gamma)^{15}$C reaction plays an important role in the discussion of neutron induced CNO cycles [5] during s-process nucleosynthesis. Such s-process scenarios are characterized by comparably low neutron densities, resulting in neutron capture times, which are slow compared to typical β decay half lives and are associated with the He and C burning phases of stellar evolution where neutrons are produced by (α,n) reactions on ^{13}C and ^{22}Ne. While the s process starts by neutron captures on iron seed nuclei, neutron captures on the light isotopes present in the burning zones can initiate a neutron induced CNO cycle. Starting from the abundant ^{12}C, the cycle is represented by the neutron capture series on ^{12}C, ^{13}C, and ^{14}C followed by the sequence $^{15}C(\beta^-)^{15}N(n,\gamma)^{16}N(\beta^-)^{16}O(n,\gamma)^{17}O(n,\alpha)^{14}$C or by producing ^{16}N via $^{14}N(n,p)^{14}C(n,\gamma)^{15}C(\beta^-)^{15}N(n,\gamma)$. The slowest reaction in this cycle is $^{14}C(n,\gamma)^{15}$C and, therefore, ^{14}C can build up a correspondingly high abundance. Although the outbreak from the neutron induced CNO cycle via $^{17}O(n,\gamma)^{18}$O is strongly suppressed by the dominance of the (n,α) channel, there might be a non-negligible effect on the neutron balance of the s process depending on the cross section for $^{14}C(n,\gamma)$. To settle this issue, the cross section would be needed for thermal energies in the 10 to 100 keV region.

Neutron capture reactions on very light nuclei carry a substantial part of the reaction flow in neutrino driven wind scenarios for the r process [6]. Among these reactions $^{14}C(n,\gamma)^{15}$C contributes mostly during the early phases, when ^{14}C is formed via the sequences ^{9}Be$(\alpha,n)^{12}C(n,\gamma)^{13}C(n,\gamma)^{14}$C and ^{9}Be$(n,\gamma)^{10}Be(\alpha,\gamma)^{14}$C. In these applications the (n,γ) cross section is required up to MeV energies because of the high temperatures in excess of 3×10^9 K, corresponding to thermal energies of about 300 keV.

The $^{14}C(n,\gamma)$ reaction is also important to validate the (n,γ) cross sections obtained by theoretical calculations [7, 8] via the Coulomb dissociation method in the experiments reported in Refs. [9, 10, 11]. In this approach the time-reversed process is measured via breakup of ^{15}C projectiles in the virtual photon field of a ^{208}Pb target. The (n,γ) cross section can then be inferred via

*present affiliation: GSI, Planckstr. 1, 64291 Darmstadt, Germany.
†present affiliation: Faculty of Science, Balqa Applied University, P.O.Box 7051, Salt 19117, Jordan.
‡present affiliation: Instituut voor Kern- en Stralingsfysica, K. U. Leuven, Celestijnenlaan 200D, B-3001 Leuven, Belgium.
§present affiliation: GSI Darmstadt, Planckstr. 1, 64291 Darmstadt, Germany.

detailed balance. The ^{14}C$(n,\gamma)^{15}$C reaction is the only case with neutrons so far where both, direct and indirect, approaches were investigated experimentally. In fact, ^{14}C belongs to the few cases where the Coulomb dissociation method can be validated in a convincingly clean way.

The first direct measurement [12] was carried out at Forschungszentrum Karlsruhe using the same sample as in the present experiment. At that time, however, the measurement was severely hampered by the fact that the nickel container used for the ^{14}C powder sample had been strongly activated by a previous irradiation with 800 MeV protons. The present study is a repetition of this first measurement after a 12-year cooling time of the nickel container, which led to a reduction of this disturbing activity to an acceptable level. Another reason for repeating the measurement was that meanwhile a more efficient detector system for the induced activity became available. Finally, the energy range was significantly extended compared to the previous experiment.

Preliminary results of this second experiment [13] turned out to be subject to significant corrections resulting from the accidental activation of the HPGe detector used. In this article we present a detailed description of the measurement as well as a thorough re-analysis of the data and of the remaining uncertainties. The results are compared to model predictions and can be used to test the applicability of the Coulomb dissociation method.

II. EXPERIMENT

A. γ-detection

The short half-life of ^{15}C of only $t_{1/2}$=2.449 $\pm$ 0.005 s [14, 15] necessitates the use of the fast cyclic activation technique [16]. The induced activity during each cycle was detected via the characteristic 5.2978 MeV γ-line (relative intensity I_γ = (63.2 $\pm$ 0.8)%) in the ^{15}C decay using a HPGe detector with a relative efficiency of 100%.

The detector efficiency was determined with a set of calibration sources and via the ^{27}Al(p,γ)^{28}Si reaction as described in Ref. [17]. The distance between the ^{15}C sample and the HPGe detector during the experiment was only 6 mm. The distance between the detector and the aluminum target during the ^{27}Al(p,γ) calibration had to be significantly increased to 76 cm in order to keep the probability for summing of different γ-rays out of one cascade at a negligible level. A thin layer of 148 nm aluminum, which corresponds to 40 μg/cm^2 as used by Anttila *et al.* [17], was evaporated on a copper backing. The thickness of the Al layer was determined with a quartz crystal. The energy loss for 1-MeV protons in this layer is less than 7 keV. The HPGe detector was placed at an angle of 55° as described in Ref. [17].

The calibration at 76 cm was completed with a set of calibrated sources, namely ^{22}Na, ^{54}Mn, ^{60}Co, and ^{208}Tl (which is part of the ^{232}Th decay chain). A separate series of calibration measurements at a distance of 6 mm to the detector was performed to normalize the above determined efficiency curve to the geometry during the cyclic activation. Very weak calibrated samples of ^{54}Mn, ^{65}Zn, ^{88}Y were used for that purpose. Simulations of the γ-ray efficiency using the detector simulation tool GEANT 3.21 [18] showed that the energy dependence is slightly different for the setup during the activation (6 mm distance) and during the ^{27}Al(p,γ)^{28}Si experiment (50 cm), see Fig. 1. This effect was taken into account during the analysis.

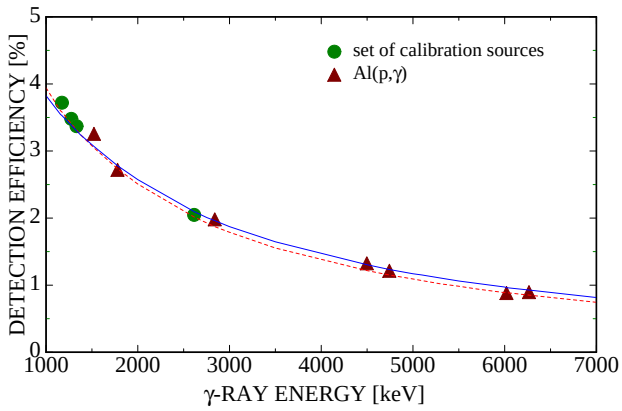

FIG. 1: (Color online) The γ-ray efficiency of the HPGe detector used during the cyclic activation. The efficiency was measured using calibration sources and the ^{27}Al(p,γ)^{28}Si reaction. The red dashed and blue solid curves correspond to GEANT simulations assuming 50 cm and 6 mm distance between sample and detector, respectively. The extrapolation from low to high energies results in slightly smaller values for the 6 mm case.

The main difference to our preliminary analysis [13] was the discovery of a huge dead time effect during the experiment. Even though the detector was shielded from the neutron production target to reduce radiation damage, enough neutrons reached the detector to produce significant intrinsic γ activity from (n,γ) reactions on ^{74}Ge and ^{76}Ge. The previous activation of the Ni container led to the production of ^{44}Ti in the container ($t_{1/2}$ = 60.3 $\pm$ 1.3 yr [19]). The 1.16 MeV γ-ray activity from the decay of the daughter ^{44}Sc was measured independently and could be used as an internal standard to determine the crucial dead time corrections of about a factor of 3.

The decay properties of the radio-nuclides used in the analysis of the efficiency calibrations are summarized in Table I. The only important change compared to the previous experiment [12] concerns the intensity of the 5297.8 MeV line in the decay of ^{15}C. The new recommended value is (63.2 $\pm$ 0.8)% [20] instead of (68 $\pm$ 2)% [21].

A 1 mm thick lead sheet was placed in front of the HPGe detector during the experiment as well as during the different calibrations in order to reduce the strong

TABLE I: Decay properties used for the determination of the detection efficiency of the HPGe detector[a] and for evaluating the ^{15}C activity [20].

Isotope	Energy (keV)	Intensity (%)
^{15}C	5297.8	63.2 ± 0.8
^{22}Na	511	181.1
	1274.5	99.94
^{44}Sc	1157.0	99.9
^{54}Mn	834.83	99.98
^{60}Co	1173.2	99.9
	1332.5	99.98
^{65}Zn	1115.5	50.6
^{88}Y	898.04	93.7
	1836.0	99.2
^{208}Tl	510.77	22.6
	583.19	84.5
	860.56	12.4
	2614.5	99.16

[a]The decay intensities of the calibration sources are known to better than 0.5% [20].

low energy background caused by bremsstrahlung from the ^{14}C decay electrons.

The results of the efficiency calibration are summarized in Table II. The photo-peak efficiency for the 5.2978 MeV line following the decay of ^{15}C was determined to (1.09 ± 0.05)%.

TABLE II: Detection efficiencies for the 5.2978 MeV decay line of ^{15}C.

Process	E (keV)	Efficiency (%)
Double Escape (DE)	4275.8	0.18 ± 0.04
Single Escape (SE)	4786.8	0.58 ± 0.06
Full Energy (FE)	5297.8	1.09 ± 0.05
Sum of all above		1.86 ± 0.09

B. Neutron spectra

Neutrons were produced via the ^{7}Li$(p,n)^7$Be reaction by bombarding metallic ^{7}Li targets with proton beams provided by the Karlsruhe 3.7 MV Van de Graaff accelerator. Different neutron energy distributions were obtained by varying of the proton energy and the thickness of the Li targets.

The thickness of the ^{14}C sample in the neutron beam direction was 5 mm . The neutron flux up- and downstream of the sample was monitored with two gold foils, allowing a measurement relative to the well known ^{197}Au$(n,\gamma)^{198}$Au cross section. At the end of each run the activity of the gold foils was determined via the 412 keV γ-ray from the ^{198}Au decay ($t_{1/2}$ = 2.7 d) using a well calibrated germanium detector. The shape of the gold foils was 21x12 mm^2 according to the activity distribution of ^{14}C in the sample, which was measured by detecting the emitted X-rays with a slit collimator.

The neutron fluxes obtained with the gold foils up- and downstream of the sample were significantly different due to the close geometry between the neutron source and the sample. This effect was evaluated by means of Monte-Carlo simulations of the neutron spectra, starting from the double-differential ^{7}Li(p,n) cross section from Liskien and Paulsen [22] and including the energy loss of the protons in the lithium layer. With this approach, the standard neutron spectrum used for activations [23] could be nicely reproduced as shown in Fig. 2.

Based on the good agreement for this spectrum, which is rather sensitive to the proton energy distribution close to the neutron production threshold, the same method was also applied to the runs at higher energies. The resulting neutron energy distributions shown in Fig. 3 represent effective spectra, where the variation of the sample thickness as a function of neutron emission angle was properly considered. Correspondingly, the neutron spectra seen by the ^{14}C sample and by the gold foils are exhibiting different widths. In addition, the spectra at 750 keV (bottom panel of Fig. 3) show a second neutron group around 200 keV, which results from the population of the first excited state in ^{7}Be at 429 keV [22]. The parameters of the different runs are summarized in Table III.

The corresponding integrated neutron fluxes are listed in Table IV. The values as derived from the gold foils were interpolated to the center plane of the sample in the following way. Since the neutron spectra for the up- and downstream gold samples differ significantly, an effective ^{197}Au(n,γ) cross section had to be calculated in a first step. This was performed by folding the effective neutron spectra with the differential ^{197}Au(n,γ) cross section by Macklin [24], normalized to Ratynski and Käppeler [23], during the Monte-Carlo simulations of the neutron spectra. The neutron flux passing the up- and downstream gold samples were then determined based on the number of produced ^{198}Au nuclei

$$\Phi = \frac{N_{198}}{N_{197} \cdot \sigma_{n,\gamma} \cdot f_b}$$

where the correction f_b accounts for the fraction of ^{198}Au nuclei that decayed already during the irradiation [25]. The flux at the sample position and the corresponding systematic uncertainties were then derived by normalizing the results from the Monte-Carlo simulations to the measured neutron fluxes at the position of the gold

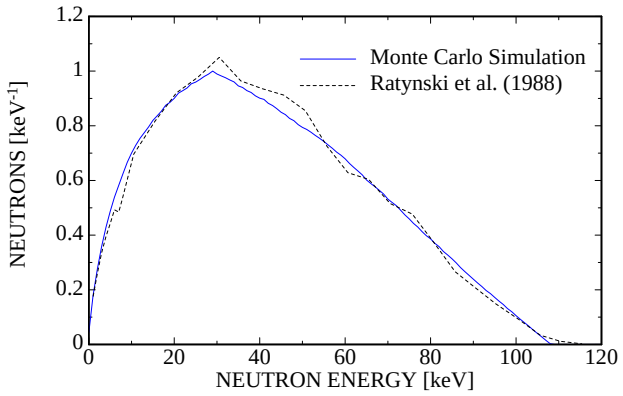

FIG. 2: (Color online) Comparison of a simulated neutron spectrum (solid, blue line) with experimental data (dashed, black line) [23] in arbitrary units.

foils:

$$
\begin{aligned}
R_{up} &= \Phi_{up}/n_{up}^{sim} \\
R_{down} &= \Phi_{down}/n_{down}^{sim} \\
R &= \left(R_{up}+R_{down}\right)/2 \\
\frac{\mathrm{d}R}{R} &= \frac{R_{up}-R_{down}}{R_{up}+R_{down}}/2 \\
\Phi_{sample} &= R\cdot n_{sample}^{sim} \\
\frac{\mathrm{d}\Phi}{\Phi} &= \frac{\mathrm{d}R}{R}
\end{aligned}
$$

TABLE III: Beam parameters and activation times of the different runs.

Run	E_p (keV)	d_{Li} (μm)	E_n (keV)	t_A (h)
I	1912	30	23.3 (MACS)	22.0
II	2001	5	150 (average)	24.0
III	2291	5	500 (average)	20.0
IV	2530	5	750 (average)	5.5

TABLE IV: Total neutron fluxes derived from the gold foils and interpolated to the center plane of the sample.

Run	Upstream		Downstream		Sample	
	σ_{up} (mbarn)	Φ_{up} (10^{13})	σ_{down} (mbarn)	Φ_{down} (10^{13})	Φ_{sample} (10^{13})	Uncert. (%)
I	604	1.82	546	1.26	1.56	3.0
II	284	2.08	270	0.62	0.84	9.4
III	155	2.42	133	1.09	1.64	6.8
IV	106	0.95	100	0.44	0.655	6.0

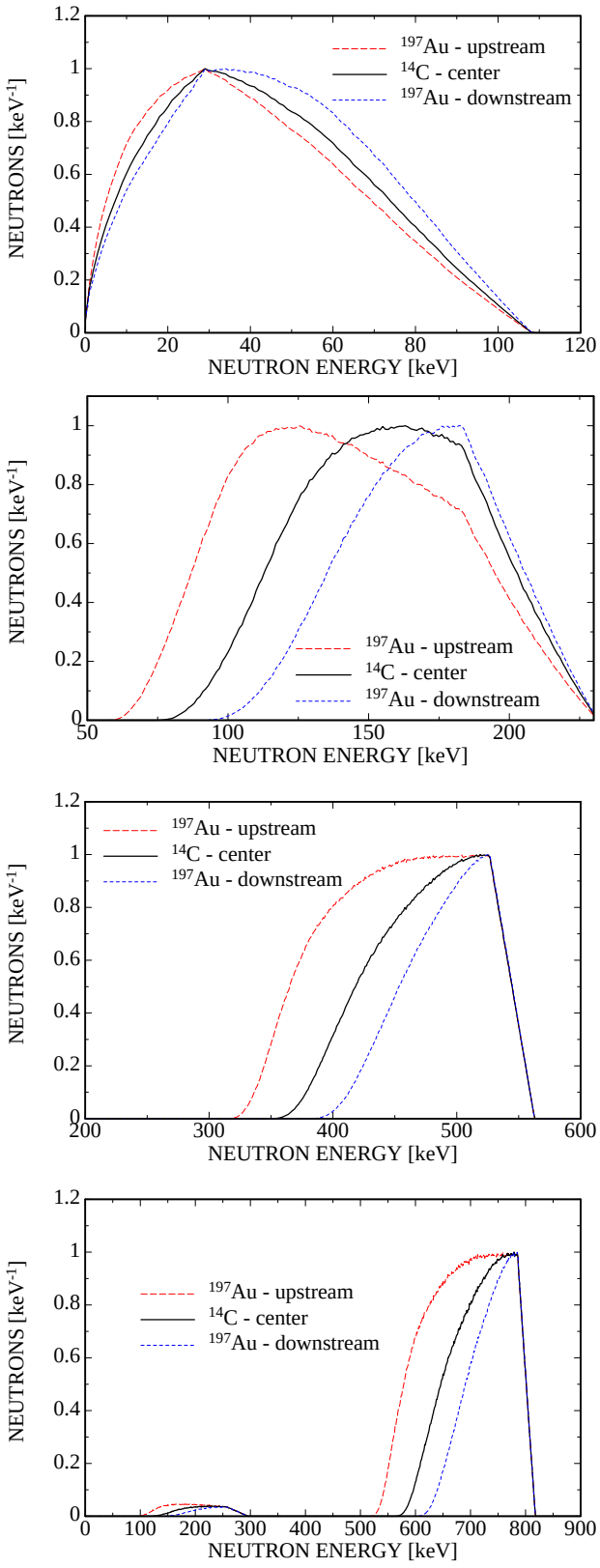

FIG. 3: (Color online) Neutron spectra for Runs I-IV (top to bottom) in arbitrary units. The curves correspond to the simulated spectra for the gold foils as well as for the ^{14}C sample. The second neutron group around 200 keV in the bottom panel results from the ^{7}Li(p,n)^{7}Be* reaction.

C. Sample mass

The independent determination of the sample mass by a calorimetric measurement of the decay heat turned out to be crucial for the analysis of this experiment. The use of this technique was favored by the comparably low β^- end point energy of $E_{max} = 156$ keV and by the fact that ^{14}C decays without emission of γ-rays. The measurement was carried out at the Tritium Laboratory of Forschungszentrum Karlsruhe [26], yielding a heat production of 370 ± 4 μW. Adopting an average energy $E_{avg} = 49.475$ keV [27] for the decay electrons and a half-life of $t_{1/2} = 5700 \pm 30$ yr [20], the measured decay heat corresponds to an activity of 1.26 ± 0.01 Ci or a total mass of 283 ± 3 mg of ^{14}C. This value is independent of the isotopic enrichment (which was quoted to be 89%) and more than a factor of two less than the specified value, which had been wrongly adopted in the previous activation [12]. This mismatch was presumably due to the undocumented removal of ^{14}C powder from the original sample.

As mentioned before, the nickel container was still slightly active due to its previous exposure to proton beams up to 800 MeV in energy. In principle, the measured decay heat of the sample represents, therefore, only an upper limit of the sample mass, since other radioisotopes can contribute as well. However, a careful analysis of all potential candidates confirms that this correction can be neglected. The two main constraints would be the half-life and the γ-activity of the contaminating isotope. Since the proton experiments were made 25 years ago, the half-life had to be in the range between 10 and 100 years, otherwise the isotope would have either already decayed or its specific activity would be too low to make any impact. The γ-activity was carefully measured by means of a HPGe detector with Be-window, and was shown not to exceed the completely negligible level of the weak ^{44}Ti decay.

D. Cyclic activation

Each cycle consisted of an activation time of $t_{beam} = 10$ s, the γ-ray detection time $t_{det} = 10$ s (during which the proton beam was switched off), and twice the time for moving the sample between detector and neutron production target $t_{wait} = 0.8$ s.

Figs. 4 and 5 show a typical γ-ray spectrum taken during the experiment. Full energy, single escape as well as double escape peaks of the 5.2978 MeV line from the decay of ^{15}C are obtained with good signal/background ratios. In order to reduce systematic uncertainties, the time dependence of the ^{15}C decay during the 10 s counting period, has been monitored. The decay curve is compared in Fig. 6 with a fit assuming a constant background and the exponential decay law with 2.449 ± 0.005 s half-life. Within the statistical uncertainties the measured activity follows the expected time dependence.

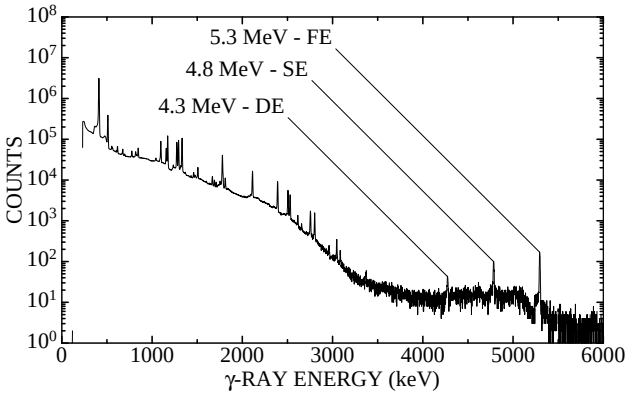

FIG. 4: Measured γ-ray spectrum after 22 h of cyclic activation during Run I (23.3 keV MACS).

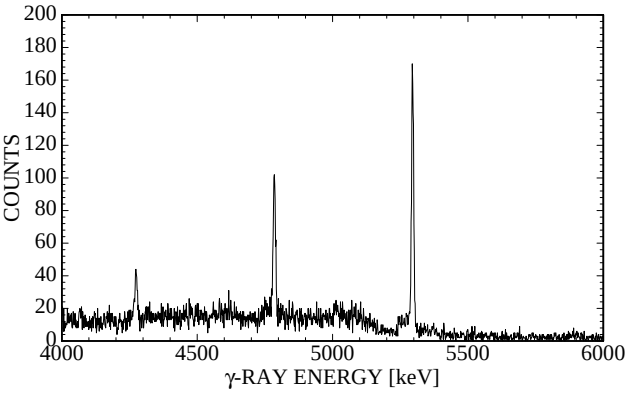

FIG. 5: The same data as shown in Fig. 4, but focused on the decay lines of ^{15}C.

III. ANALYSIS AND RESULTS

A. Results from the activation measurement

The ^{14}C(n,γ) cross section for the different neutron spectra were determined from the ratio of ^{15}C to ^{14}C atoms including corrections for ^{15}C atoms decayed, while the sample was not in front of the HPGe detector. The details of this method are very well described in [12, 28]. The results including uncertainties are presented in Table V. The main contributions to the overall uncertainty come from counting statistics (2-8%), the γ-ray detection efficiency (5%), and the determination of the neutron flux (2-10%). All other uncertainties are smaller than 2%. With respect to the second neutron group during Run IV (750 keV), we performed the entire analysis three times. A first time without consideration of the second group, a second time with the cross section as suggested by [22], and a last time adopting twice the cross section populating the excited state of ^{7}Be. The value for the resulting ^{14}C(n,γ) cross section increased by 5% in each step. Therefore we quadratically added

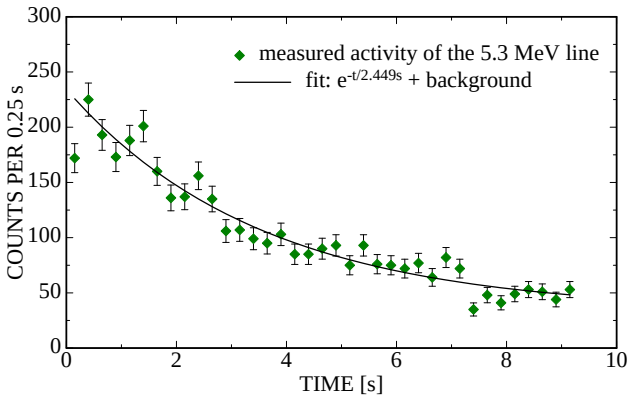

FIG. 6: (Color online) Time dependence of the ^{15}C activity.

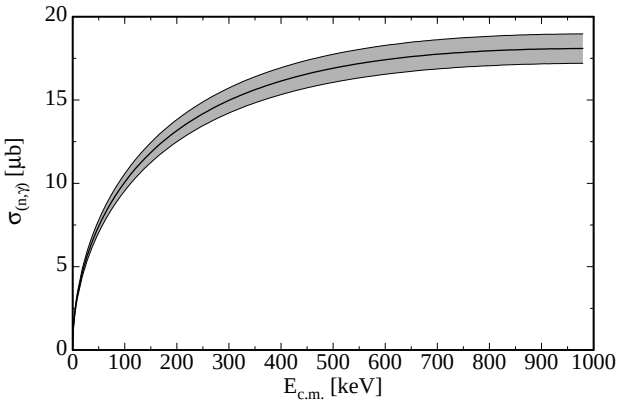

FIG. 7: Theoretical ^{14}C$(n,\gamma)^{15}$C cross section, fitted to the experimental data, as described in the text.

an additional systematic uncertainty of 5% to the cross section at 750 keV.

B. Theoretical modeling of direct radiative capture

We used a simple potential model to calculate the cross section for direct capture of a low-energy neutron on ^{14}C. The modeling of this radiative process was further simplified by relying on Siegert's theorem to approximate the exact current form ($\mathbf{j}\cdot\mathbf{A}$) of the electromagnetic operator by its density form in terms of electrostatic multipoles. The calculations were performed with the direct-reaction code FRESCO [29], and the radiative capture was modeled as a one-step process using first-order DWBA theory. A real potential was used to describe the incident wave, which is appropriate for capture far from resonances, and to generate the single-particle configurations of the ground and first-excited states of ^{15}C (bound $1s_{1/2}$ and $0d_{5/2}$, respectively). These two states are very close to pure single-particle configurations, which validates our potential-model approach. Since we assume that the observed, non-resonant cross section corresponds to direct radiative capture, the calculated cross section only had to be normalized by the final bound-state spectroscopic factor. The ratio of experimentally observed to calculated cross section is then a measure of the spectroscopic purity of the single-particle configuration. We note that the particular structure of the ^{15}C states implies that E1 capture is only possible for p-wave neutrons. The possibility of E2 capture of s-wave neutrons to the first-excited state was also included in these calculations, but the contribution to the capture cross section was found to be less than 5% at the relevant energies.

In all calculations, single-particle configurations were generated from a Woods-Saxon potential well with the geometry of Ref. [30]. The potential depths were chosen to reproduce the binding energies of the two bound states in ^{15}C with respect to the ^{14}C+n thresholds. This procedure led to slightly different potential depths for the $l = 0$ ($V_{l=0} = 52.81$ MeV) and $l > 0$ ($V_{l>0} = 51.33$ MeV) channels. Since p-wave capture is the dominating process, the $l > 0$ potential was used to describe the scattering wave of the incoming channel. The use of l-dependent potentials is, in principle, not compatible with the requirements of applying Siegert's theorem. However, for the case considered here, we found that the difference between the initial- and final-state potentials was so small that Siegert's theorem was still valid.

The calculated radiative-capture cross section was convoluted with the neutron spectra of Fig. 3 to facilitate a direct comparison with the data from the activation measurement. The calculated capture to the first excited state of ^{15}C was normalized by the spectroscopic factor $C^2S_1 = 0.69$, extracted from experimental neutron transfer ^{14}C$(d,p)^{15}$C* data [31]. Since this channel contributes less than 5% to the total capture cross section at the relevant energies, the final result is not very sensitive to the particular choice of this spectroscopic factor. A fit to the experimental data, weighted by the relative error bar of each data point, was then performed and resulted in a best-fit spectroscopic factor of $C^2S_0 = 0.95 \pm 0.05$ for the ground state $1s_{1/2}$ single-particle configuration, which is in good agreement with 0.88 as derived from (d,p) data [31]. The final calculated cross section, convoluted with the different neutron spectra, is compared with the experimental data in Table V. In addition, the energy-differential cross section, including the 1σ error band, is shown in Fig. 7.

C. Recommended astrophysical reaction rates

The fitted theoretical cross section of the previous section was used to compute reaction rates for astrophysical applications. The resulting reaction rate is plotted in Fig. 8 as a function of stellar temperature T_9 (in units of 10^9 K). The applicability of the calculated capture cross section is restricted by the experimental energy range

TABLE V: Cross sections of the $^{14}C(n,\gamma)^{15}C$ reaction.

Run	Neutron energy distribution (keV)	Cross section results (μbarn)		
		Measured values[a]	Theory[b]	Theory/Experiment
I	23.3 (MACS)	7.1±0.5 (6.7)	6.5 ± 0.4	0.92 ± 0.08
II	150 (average)	10.7±1.2 (11)	11.7 ± 0.6	1.09 ± 0.12
III	500 (average)	17.0±1.5 (8.8)	16.5 ± 0.8	0.97 ± 0.10
IV	750 (average)	15.8±1.6 (10)	17.5 ± 0.9	1.11 ± 0.11

[a] Relative uncertainties (in %) are indicated in brackets.
[b] Convoluted with the neutron spectra of Fig. 3.

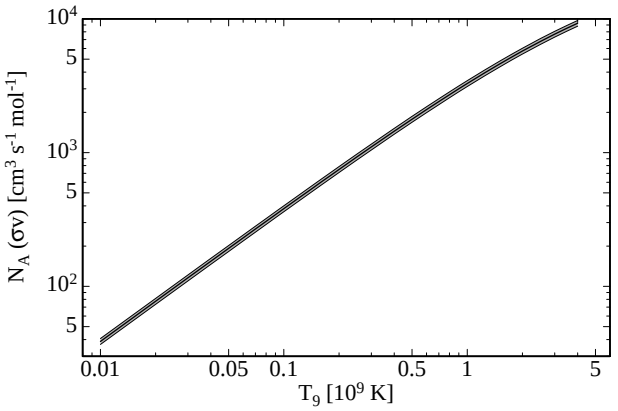

FIG. 8: Reaction rates for $^{14}C(n,\gamma)^{15}C$ as a function of stellar temparature T_9 given in 10^9 K.

used in the activation measurement, i.e. from 1 keV to 1 MeV. The extracted reaction rate is therefore presented up to a maximum temperature of $4 \cdot 10^9$ K. Extrapolations beyond this temperature range would yield results that are not restricted by the data from the present experiment.

The reaction rates were fitted to the parametrization suggested by Rauscher and Thielemann [32]

$$N_A\langle\sigma v\rangle = \exp\Big(a_1 + a_2 T_9^{-1} + a_3 T_9^{-1/3} + a_4 T_9^{1/3} + a_5 T_9 + a_6 T_9^{5/3} + a_7 \ln(T_9)\Big).$$

The reaction rate is given in cm^{3}s^{-1}mol^{-1} with the temperature in 10^9 K. The best-fit parameters, which reproduce the numerical values to within 0.01% in the $0.01 \le T_9 \le 4.0$ temperature range, are:

$$\begin{aligned} a_1 &= 0.850 \cdot 10^1 \\ a_2 &= -0.305 \cdot 10^{-3} \\ a_3 &= 0.580 \cdot 10^{-1} \\ a_4 &= -0.355 \cdot 10^0 \\ a_5 &= -0.116 \cdot 10^0 \\ a_6 &= 0.122 \cdot 10^{-1} \\ a_7 &= 0.109 \cdot 10^1 \end{aligned}$$

IV. DISCUSSION AND ASTROPHYSICAL IMPLICATIONS

Compared to the result of the previous activation with $kT = 23.3$ keV [12] ($1.72 \pm 0.43\ \mu$b) we find agreement, if the sample mass measured in this work and the currently available decay properties of ^{15}C are taken into account. The agreement is then within 1σ.

All available differential data for the total capture cross section of ^{14}C are compared in Fig 9. The data are divided by $\sqrt{E}$ to remove the energy dependence caused by the p-wave orbital-momentum barrier. The present cross section results are in good agreement with theoretical estimates of Wiescher *et al.* [7] and with the recently published estimates of Timofeyuk *et al.* [8] based on mirror symmetry considerations. Our data fall approximately 20% below the values of Descouvemont [33], but exhibit the same energy dependence.

The results of Horváth *et al.* [9], which were obtained in a Coulomb-breakup study, show a large, constant offset (Fig 9). In other words, not only the cross section values are different, but also the energy dependence. The difference can be expressed as:

$$\begin{aligned} \sigma_{present} &= \sigma_{Horvath} + c \cdot \sqrt{E_{c.m.}} \\ \text{with } c &= 0.48\ \mu\text{b/keV}^{1/2} \end{aligned}$$

With respect to the importance of the $^{14}C(n,\gamma)^{15}C$ cross section for validating the Coulomb-break-up approach for

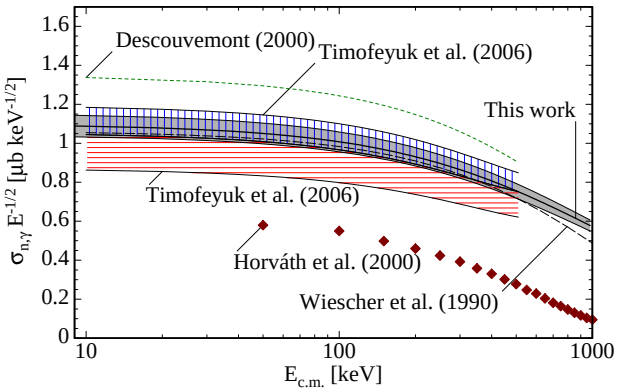

FIG. 9: (Color online) Comparison between the present results and previous data.

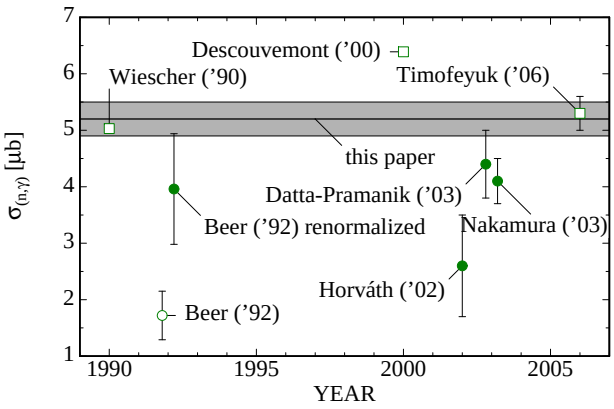

FIG. 10: (Color online) Comparison between this measurement (shaded band) and previous cross section results at $E_{c.m.} = 23.3$ keV. Open squares refer to theoretical estimates while full circles refer to experiments including Coulomb-breakup studies. The only open circle refers to the measurement by Beer *et al.* before the renormalization based on the new mass and line intensity information (see text). The respective references from left to right are [7],[33],[8] (theoretical) and [12], [9],[10, 35],[11, 34] (experimental).

deducing this cross section from the time-reversed dissociation of ^{15}C it is important, however, to emphasize that the present results are in good agreement with preliminary data from two other Coulomb break-up studies [10, 11, 34].

Since the paper by Beer *et al.* [12], a comparison of the differential cross section at 23.3 keV is published in most papers dealing with the $^{14}C(n,\gamma)$ cross section. We note that the value published by Beer *et al.* was a Maxwellian averaged cross section for $kT = 23.3\ keV$, which is different from the differential cross section at $E_{c.m.} = 23.3$ keV. In this tradition, a comparison of the differential 23.3 keV cross sections is presented in Fig. 10. The present value of 5.2 ± 0.3 μbarn is based on the theoretical description of the cross section provided in the previous section.

The rate suggested by [7] has been used for most of the nucleosynthesis simulations of the scenarios summarized at the beginning of this paper. The agreement with the present experimental results confirms many of the previous model predictions. While present Cosmologies dismiss the likelihood of inhomogeneous Big Bang scenarios, previous simulations of the associated nucleosynthesis [36] based on this $^{14}C(n,\gamma)$ reaction rate demonstrated a substantial production of ^{14}C at such conditions.

The role of the $^{14}C(n,\gamma)^{15}C$ reaction as the slowest link in the neutron induced CNO cycles proposed by [5] is also confirmed by the present results. Detailed simulations now help to analyze the impact of such a cycle on the neutron flux during core carbon burning and shell carbon burning. These results indicate that many more branches exist due to the presence of charged particles in stellar helium and carbon burning environments [37]. For helium burning most of the ^{13}C produced by $^{12}C(n,\gamma)$ is depleted by the $^{13}C(\alpha,n)$ reaction rather than by $^{13}C(n,\gamma)$ and the production of ^{14}C is negligible as shown already by [38]. This may be different for shell carbon burning which is characterized by higher ^{12}C abundances and a significantly lower α flux. New simulations on aspects of neutron production and capture reactions are presently in preparation [39]. The study indicates that the main production of ^{14}C is given by the two reactions $^{14}N(n,p)^{14}C$ and $^{17}O(n,\alpha)^{14}C$. Because of the here confirmed low cross section, the $^{14}C(n,\gamma)$ reaction does not play a significant role for reducing the ^{14}C abundance. However, because of the relatively high temperatures of T≈1 GK in the carbon burning zone, alternative depletion channels open via $^{14}C(p,n)^{14}N$ with a negative Q-value of -626 keV and via $^{14}C(\alpha,\gamma)^{18}O$ alpha capture providing a new abundance balance.

New simulations are also underway for studying the impact of neutron capture reactions on neutron rich Be, B, and C isotopes on the nucleosynthesis of light elements in neutrino driven wind supernova shock scenarios [40]. The completion of these studies does however require a detailed analysis of neutron capture reactions on short-lived neutron rich isotopes to simulate the anticipated reaction flow reliably [6]. New shell model based simulations of these rates are presently in preparation taking also into account the rapidly growing experimental nuclear structure information on neutron rich nuclei in the Be to Ne range.

V. SUMMARY

We have measured the $^{14}C(n,\gamma)^{15}C$ cross section applying the activation technique with four different energy distributions. The results of the present experiment has removed the uncertainty associated with the results of the previous $^{14}C(n,\gamma)$ activation measurement by [25]. A

theoretical fit of the present cross section data is in good agreement with the capture cross sections deduced from Coulomb dissociation studies of ^{15}C beams by [10] and [11] while in striking disagreements with a third measurement by [9]. Moreover, our results and analysis demonstrate good agreement with a number of theoretical predictions for the reaction rate by [7] and [8].

The experimental results confirm the rate suggested by [7], which has been used for most of the nucleosynthesis simulations mentioned in the Sec. I. Therefore, the astrophysical consequences of the previous model predictions remain essentially unchanged. A new aspect concerning the role of neutron capture reactions on neutron rich Be, B, and C isotopes is the production of light elements in neutrino driven wind supernova shock scenarios, which are presently under investigation [40].

Acknowledgments

We would like to thank E.-P. Knaetsch, D. Roller, and W. Seith for their support at the Karlsruhe Van de Graaff accelerator. We are also grateful to M. Pignatari for discussing the impact of our experimental results on the ^{14}C nucleosynthesis during stellar helium and carbon burning. This work was partly supported by the Joint Institute for Nuclear Astrophysics (JINA) through NSF Grants Nos. PHY-0072711 and PHY-0228206, and partly performed under the auspices of the U.S. Department of Energy by the University of California, Lawrence Livermore National Laboratory (LLNL) under contract No. W-7405-Eng-48 and the Los Alamos National Laboratory (LANL) under the auspices of Los Alamos National Security, LLC, DOE contract number DE-AC52-06NA25396.

[1] J. H. Applegate and C. J. Hogan, Phys. Rev. D (Particles and Fields) **31**, 3037 (1985).
[2] J. H. Applegate, C. J. Hogan, and R. J. Scherrer, Astrophysical Journal **329**, 572 (1988).
[3] R. A. Malaney and W. A. Fowler, Ap. J. **333**, 14 (1988).
[4] F. Ajzenberg-Selove, Nucl. Phys. A **449**, 1 (1986).
[5] M. Wiescher, J. Görres, and H. Schatz, Journal of Physics G Nuclear Physics **25**, 133 (1999).
[6] M. Terasawa, K. Sumiyoshi, T. Kajino, G. J. Mathews, and I. Tanihata, Astrophys. J. **562**, 470 (2001).
[7] M. Wiescher, J. Görres, and F.-K. Thielemann, Ap. J. **363**, 340 (1990).
[8] N. K. Timofeyuk, D. Baye, P. Descouvemont, R. Kamouni, and I. J. Thompson, Phys. Rev. Let. **96**, 162501 (2006).
[9] A. Horváth, J. Weiner, A. Galonsky, F. Deák, Y. Higurashi, K. Ieki, Y. Iwata, A. Kiss, J. Kolata, Z. Seres, et al., Ap. J. **570**, 926 (2002).
[10] U. Datta Pramanik, T. Aumann, K. Boretzky, B. Carlson, D. Cortina, T. Elze, H. Emling, H. Geissel, A. Grünschloß, M. Hellström, et al., Phys. Lett. B **551**, 63 (2003).
[11] T. Nakamura, N. Fukuda, N. Aoi, H. Iwasaki, T. Kobayashi, T. Kubo, A. Mengoni, M. Notani, H. Otsu, H. Sakurai, et al., Nuclear Physics A **722**, 301 (2003).
[12] H. Beer, M. Wiescher, F. Käppeler, J. Görres, and P. E. Koehler, Ap. J. **387**, 258 (1992).
[13] R. Reifarth, M. Heil, R. Plag, U. Besserer, S. Dababneh, L. Dörr, J. Görres, R. C. Haight, F. Käppeler, A. Mengoni, et al., Nucl. Phys. A **758**, 787C (2005).
[14] D. E. Alburger and D. J. Millener, Phys. Rev. C **20**, 1891 (1979).
[15] G. Audi, O. Bersillon, J. Blachot, and A. H. Wapstra, Nucl. Phys. A **624**, 1 (1997).
[16] H. Beer, Ap. J. **375**, 823 (1991).
[17] A. Anttila, J. Keinonen, M. Hautala, and I. Forsblom, NIM **147**, 501 (1977).
[18] J. Apostolakis, Tech. Rep., CERN, GEANT library (1993), http://wwwinfo.cern.ch/asd/geant/.
[19] J. Görres, J. Meißner, H. Schatz, E. Stech, P. Tischhauser, M. Wiescher, D. Bazin, R. Harkewicz, M. Hellström, B. Sherrill, et al., Physical Review Letters **80**, 2554 (1998).
[20] R. B. Firestone, *Table of Isotopes* (Wiley, New York, 1996).
[21] E. Browne and R. Firestone, *Table of Radioactive Isotopes* (Wiley, New York, 1986).
[22] H. Liskien and A. Paulsen, Atomic Data and Nucl. Data Tables **15**, 57 (1975).
[23] W. Ratynski and F. Käppeler, Phys. Rev. C **37**, 595 (1988).
[24] R. Macklin (1982), private communication to Mughabghab, S.F.
[25] H. Beer and F. Käppeler, Phys. Rev. C **21**, 534 (1980).
[26] L. Dörr, U. Besserer, M. Glugla, S. Grünhagen, B. Kloppe, M. Sirch, and J. Hemmerich, Fusion Sci. Tech. **48**, 358 (2005).
[27] Tech. Rep., Brookhaven National Laboratory (2007), online Nuclear Data Files NUDAT: www.nndc.bnl.gov/nudat2/.
[28] H. Beer, G. Rupp, G. Walter, F. Voss, and F. Käppeler, Nucl. Instr. Meth. A **337**, 492 (1994).
[29] I. J. Thompson, Comp. Phys. Rep. **7**, 167 (1988).
[30] P. Capel, D. Baye, and V. S. Melezhik, Phys. Rev. C **68**, 014612 (2003).
[31] J. D. Goss, P. L. Jolivette, C. P. Browne, S. E. Darden, H. R. Weller, and R. A. Blue, Phys. Rev. C **12**, 1730 (1975).
[32] T. Rauscher and F.-K. Thielemann, Atomic Data Nucl. Data Tables **75**, 1 (2000).

[33] P. Descouvemont, Nuclear Physics A **675**, 559 (2000).
[34] T. Nakamura (2004), private communication.
[35] U. D. Pramanik and Land-Cb-Frs-Collaboration, Progress of Theoretical Physics Supplement **146**, 427 (2002).
[36] T. Rauscher, J. Applegate, J. Cowan, F.-K. Thielemann, and M. Wiescher, Ap. J. **429**, 499 (1994).
[37] M. Pignatari, R. Gallino, M. Heil, M. Wiescher, F. Käppeler, F. Herwig, and S. Bisterzo, Ap. J. **in prep.** (2007).
[38] C. Travaglio, R. Gallino, C. Arlandini, and M. Busso, MemSAIt **67**, 831 (1996).
[39] M. Pignatari, R. Gallino, M. Wiescher, and F. Herwig, Ap. J. **in prep.** (2008).
[40] A. Bartlett, J. Görres, G. J. Mathews, K. Otsuki, M. Wiescher, D. Frekers, A. Mengoni, and J. Tostevin, Phys. Rev. C **74**, 015802 (2006).